Bioactive Materials 6 (2021) 179–190

Contents lists available at ScienceDirect

Bioactive Materials

journal homepage: http://www.keaipublishing.com/biomat

A 3D-Bioprinted dual growth factor-releasing intervertebral disc scaffold induces nucleus pulposus and annulus fibrosus reconstruction

Binbin Sun[a,b], Meifei Lian[c], Yu Han[a,b], Xiumei Mo[d], Wenbo Jiang[b], Zhiguang Qiao[a,b,e,**], Kerong Dai[a,b,*]

[a] Department of Orthopaedic Surgery, Shanghai Key Laboratory of Orthopaedic Implants, Shanghai Ninth People's Hospital, Shanghai Jiao Tong University School of Medicine, Shanghai, 200080, China
[b] Clinical and Translational Research Center for 3D Printing Technology, Shanghai Ninth People's Hospital, Shanghai Jiao Tong University School of Medicine, Shanghai, 200011, China
[c] Department of Prosthodontics, Shanghai Ninth People's Hospital, College of Stomatology, Shanghai Jiao Tong University School of Medicine, National Clinical Research Center for Oral Diseases, Shanghai Key Laboratory of Stomatology & Shanghai Research Institute of Stomatology, Shanghai, 200011, China
[d] State Key Lab for Modification of Chemical Fibers & Polymer Materials, College of Chemistry, Chemical Engineering and Biotechnology, Donghua University, Shanghai, 201620, China
[e] Department of Orthopaedic Surgery, Renji Hospital, South Campus, Shanghai Jiao Tong University School of Medicine, Shanghai, 201112, China

ARTICLE INFO

Keywords:
Intervertebral disc (IVD)
Regenerative medicine
3D bioprinting
Mesenchymal stem cells (MSCs)
Growth factor (GF)

ABSTRACT

Regeneration of Intervertebral disc (IVD) is a scientific challenge because of the complex structure and composition of tissue, as well as the difficulty in achieving bionic function. Here, an anatomically correct IVD scaffold composed of biomaterials, cells, and growth factors were fabricated via three-dimensional (3D) bioprinting technology. Connective tissue growth factor (CTGF) and transforming growth factor-β3 (TGF-β3) were loaded onto polydopamine nanoparticles, which were mixed with bone marrow mesenchymal stem cells (BMSCs) for regenerating and simulating the structure and function of the nucleus pulposus and annular fibrosus. *In vitro* experiments confirmed that CTGF and TGF-β3 could be released from the IVD scaffold in a spatially controlled manner, and induced the corresponding BMSCs to differentiate into nucleus pulposus like cells and annulus fibrosus like cells. Next, the fabricated IVD scaffold was implanted into the dorsum subcutaneous of nude mice. The reconstructed IVD exhibited a zone-specific matrix that displayed the corresponding histological and immunological phenotypes: primarily type II collagen and glycosaminoglycan in the core zone, and type I collagen in the surrounding zone. The testing results demonstrated that it exhibited good biomechanical function of the reconstructed IVD. The results presented herein reveal the clinical application potential of the dual growth factors-releasing IVD scaffold fabricated via 3D bioprinting. However, the evaluation in large mammal animal models needs to be further studied.

1. Introduction

Low back pain (LBP) is an age-related chronic disease and its socioeconomic cost is increasing with population aging [1,2]. In clinical practice, both invasive surgical procedures (spine fusion or arthroplasty) and regarding arthroplasty (total disc replacement) were used to treat LBP. However, both of these treatment approaches have their limitations: high cost, low success rate, long recovery time, and development of late complications several years after the procedures [3–5]. Recently, growing number of researchers focus on the use of biocomposite materials to fabricate intervertebral disc (IVD) scaffold for disc repair.

IVDs are fibrocartilaginous tissues important for spinal function, as they provide stability between vertebrae while permitting motion [6]. IVD is a complex structure primarily composed of three types of tissues: the nucleus pulposus (NP) and the annulus fibrosus (AF) and cartilage

Peer review under responsibility of KeAi Communications Co., Ltd.
* Corresponding author. Department of Orthopaedic Surgery, Shanghai Key Laboratory of Orthopaedic Implants, Shanghai Ninth People's Hospital, Shanghai Jiao Tong University School of Medicine, Shanghai, 200080, China.
** Corresponding author. Department of Orthopaedic Surgery, Shanghai Key Laboratory of Orthopaedic Implants, Shanghai Ninth People's Hospital, Shanghai Jiao Tong University School of Medicine, Shanghai, 200080, China.
E-mail addresses: dr_qiaozhiguang@126.com (Z. Qiao), krdai@163.com (K. Dai).

https://doi.org/10.1016/j.bioactmat.2020.06.022
Received 8 April 2020; Received in revised form 28 June 2020; Accepted 28 June 2020

endplates. As the two most important parts, the structure and composition of NP and AF are different, and they performed different functions. The NP is primarily composited of glycosaminoglycan (GAG) and type II collagen (Col II) fibers. It forms the hydrogel-like hyaline cartilage tissue that exerts an elastic function to distribute hydraulic pressure. As the core of IVD, the NP is surrounded by the AF. The AF is composed of type I collagen (Col I) fibers and forms the cricoid fibrocartilage. It helps withstand compressive forces and hold the NP in place during compression [7,8]. Therefore, for IVD reconstruction, the research endpoint is to achieve successful reconstruction and functional recovery of both AF and NP tissues through the biomimetic structure and composition of IVD.

In fact, although several groups have attempted to reconstruct IVDs with different materials and methods, few can reproduce the hierarchical structure and function of native IVDs [9,10]. In the Yang et al. report, an IVD scaffold was fabricated by reverse reconstruction method to obtain structural bionics [11]. However, the IVD scaffold was prepared with nonbiodegradable materials (bacterial cellulose) and lacked the necessary biological activities. Many studies have confirmed that cells and growth factors (GFs) were essential for providing the biological activity of IVD scaffolds [12]. GFs such as basic fibroblast growth factor (bFGF) [13], bone morphogenic protein-2 (BMP-2) [14], and transforming growth factor-β (TGF-β) superfamily [15–17], have been investigated, while both NP cells [18] and induced pluripotent stem cells (iPSC) are widely used to repair IVDs [6]. Mesenchymal stem cells (MSCs) show a higher potential for IVD application because of the wide range of sources, low immunogenicity, and strong differentiation capacity.

MSCs have been proven to possess the ability to differentiate into chondrocytes [19]. Notably, MSCs may differentiate into pulposus like cells and annulus fibrosus like cells via induction with connective tissue growth factor (CTGF) and TGF-β3, respectively [20]. In the study of Lee et al., CTGF and TGF-β3 were loaded and released from the different sites of a meniscus scaffold for knee meniscus reconstruction via inducing fibrochondrocytic differentiation of endogenous cells [20]. Therefore, we hypothesized that through mixing of CTGF and TGF-β3 with MSCs and loading onto the AF and NP regions of an IVD scaffold could lead to the differentiation of the corresponding MSCs into fibrocartilage and hyaline cartilage like tissues, respectively. In addition, the release system of GFs is important when fabricating an IVD scaffold. Polydopamine nanospheres (PDA NPs) are ideal carriers for GFs because of two reasons: many active functional groups exist on the surface of PDA NPs that can be used to graft the GFs, and the excellent adhesion properties of PDA NPs can promote the delivery of GFs [21]. However, the fabrication of IVD scaffolds with such complex structures and components, which include cells, GFs, and biomaterials, are difficult to achieve using conventional methods.

Three-dimensional (3D) bioprinting is a novel technology that has shown great potential and enormous advantages in IVD repair. As a personalized, flexible, and precise technology, 3D bioprinting can achieve precise bionics according to the structure and size of native tissues and organs [22]. In addition, 3D bioprinting allows not only the printing of a combination of biomaterials but also the accurate placement of cells and GFs [23,24]. However, 3D bioprinting technology is a relatively new approach for the preparation of tissue engineering scaffold, and most current studies simply combine the biomaterials with cells/GFs [25]. Since the required equipment and printing parameters of biomaterials, cells, and GFs are different, the printing of IVD scaffolds comprising all these components can be major challenge with regard to both the construction and design of the 3D bioprinting system.

Here, we report a novel approach and design to prepare an anatomically correct IVD scaffold with biomaterials, cells, and GFs using 3D bioprinting technology. The core of the IVD scaffold was printed by mixing bone marrow mesenchymal stem cells (BMSCs) and TGF-β3 with hydrogel to simulate the structure and function of the NP, while the surrounding tissue AF was printed by mixing BMSCs and CTGF with hydrogel. In addition, the biomaterial polycaprolactone (PCL) was used to print the framework of the whole IVD scaffold to provide the necessary mechanical support. The dual GFs were loaded onto PDA NPs, which were shown to exhibit stable and effective release behavior. The IVD scaffold released the two types of GFs in a spatially and temporally controlled manner, leading to the reconstruction of different tissue phenotypes. *In vitro* and *in vivo* experiments were performed to evaluate the clinical potential of the 3D-bioprinted IVD scaffold. Data presented herein provide constructive clues for the application of 3D bioprinting in IVD tissue reconstruction.

2. Materials and methods

2.1. Materials

Dopamine (DA) and tris-(hydroxymethyl)-aminomethane (Tris) were purchased from Sigma-Aldrich (USA). Concentrated hydrochloric acid (HCl) was obtained from Sinopharm Chemical Reagent Co., Ltd (China). Polymer PCL (molecular weight = 45 kDa) was purchased from Sigma-Aldrich (USA). Gelatin (Gel), hyaluronic acid (HA), sodium alginate (SA), and calcium chloride anhydrous ($CaCl_2$) were purchased from Aladdin Co., Ltd. (China). CTGF (recombinant, rat) was purchased from R&D systems (USA) and TGF-β3 (recombinant, rat) was purchased from ProSpec (USA). Cell culture reagents, such as Dulbecco's Modified Eagle Medium (DMEM), fetal bovine serum (FBS), and trypsin were purchased from Life Technologies (USA). The Rat (SD) Mesenchymal Stem Cell Chondrogenic Differentiation Basal Medium was purchased from Cyagen Biosciences Inc. (China). BMSCs were extracted from the bone marrow of Sprague Dawley (SD) rats. SD rats and nude mice were obtained from the Animal Laboratory Center of Shanghai Jiao Tong University (China).

2.2. Preparation of PDA NPs and loading of GFs on PDA NPs

PDA NPs were prepared through chemical oxidative polymerization according to a previous report [21]. In brief, Tris-HCl buffer solution with a determined degree of acidity (pH = 9) was first prepared. The Tris-HCl buffer was then mixed with isopropanol at a volume ratio of 4:1, and then the mixed solution was filtered through a polytetrafluoroethylene (PTFE) membrane filter (0.45 μm, China) to remove impurities. Next, DA monomers at a final concentration of 10 mg/mL was added. The mixture was subjected to 9 h of constant stirring to allow for oxidative polymerization, after which PDA NPs were obtained. The PDA NPs were then centrifuged for 20 min at 10 000 rpm in a high-speed refrigerated benchtop centrifuge (Neofuge-18Rr, China), and the supernatant was discarded. Afterwards, the PDA NPs were washed three times with deionized water. Subsequently, CTGF and TGF-β3 were loaded onto the surface of the PDA NPs through covalent binding. Briefly, a total of 10 mg PDA NPs were resuspended in 1 mL of deionized water. Separately, a 200 mg/mL EDC/NHS (5:3, w/w) solution was prepared. Then, CTGF (10 μg/mL) or TGF-β3 (2.5 μg/mL) were mixed with the PDA NPs suspension and EDC/NHS solution according to the volume ratio of CTGF (or TGF-β3): EDC/NHS: PDA NPs: deionized water = 3:1:4:2. The CTGF@PDA NPs and TGF-β3@PDA NPs were obtained after shaking at 4 °C for 6 h. Subsequently, the GF–loaded PDA NPs were centrifuged (10 000 rpm, 20 min) and washed with deionized water three times and resuspended in phosphate-buffered saline (PBS) solution for subsequent experiments.

2.3. Characterization of PDA NPs and GF-loading efficiency

The centrifuged PDA NPs, CTGF@PDA NPs, and TGF-β3@PDA NPs were resuspended in ethanol and sonicated for 5 min. After the ethanol had evaporated, the samples were examined using a scanning electron microscope (SEM). The particle size of the samples was measured using a laser particle size analyzer (Mastersizer, UK), and the particle size

distribution images were obtained. The characteristics of the raw DA, prepared PDA NPs, CTGF@PDA NPs, and TGF-β3@PDA NPs were evaluated using Fourier transform infrared spectroscopy (FTIR) and Raman spectroscopy (RS). Infrared measurements were performed in an FTIR spectrometer (Thermo Fisher 6700, USA) at a wavenumber range from 4000 to 400 cm^{-1}. Raman measurements were performed in a laser Raman spectrometer (Renishaw, UK) at a wavenumber range from 3200 to 400 cm^{-1}. The loading efficiency of CTGF and TGF-β3 was measured using the difference method. Briefly, the concentration of the residual GFs retained in the supernatant was quantified using the corresponding ELISA Kit (R&D Systems, USA), and the loading efficiency of CTGF and TGF-β3 was calculated by the differences between the values obtained from the ELISA and the respective initial concentrations of the GFs.

2.4. Preparation of 3D bioprinting inks

Through preliminary testing, a 3D bioprinting ink that allowed GF-release and cell-loading was prepared by mixing the CTGF@PDA NPs (or TGF-β3@PDA NPs), BMSCs, and hydrogel. The BMSCs were extracted from 20 SD rats (4–6-week-old, purchased from Animal Laboratory Center of Shanghai Jiao Tong University, China) according to a previously reported protocol. The BMSCs were cultured in DMEM/F-12 medium supplemented with 15% FBS and 1% penicillin-streptomycin formulation at 37 ˚C with 5% CO_2 in a humidified atmosphere. After culturing and proliferation, the BMSCs at passage 2 (P2) were used to prepare the 3D bioprinting ink. The hydrogel was prepared by dissolving Gel, SA, and HA in DMEM at 50 ˚C and stirred for 2 h. The procedure resulted in the following final concentrations: Gel (200 mg/mL), SA (100 mg/mL), HA (100 mg/mL), and Glycerol (100 mg/mL). The prepared solution was sterilized by passing through a 0.45-μm syringe filter, and the temperature of the solution was reduced to 37 ˚C. BMSCs and CTGF@PDA NPs (or TGF-β3@PDA NPs) were mixed with the hydrogel at 37 ˚C to obtain the respective 3D bioprinting ink (the CTGF/BMSCs ink and the TGF-β3/BMSCs ink). The cell density of BMSCs was 1×10^7 cells/mL, and the final concentration of CTGF@PDA NPs (or TGF-β3@PDA NPs) was 10 mg/mL. The CTGF@PDA NPs (or TGF-β3@PDA NPs) were sterilized under ultraviolet (UV) light for 2 h before mixing. All of the experimental procedures were performed under sterile conditions.

2.5. Designing of 3D model and bioprinting of IVD scaffold

Before bioprinting, a 3D model of the IVD scaffold was designed using the AutoCAD software. The model was divided into five parts, which corresponded to the upper cartilage endplate (UCE), lower cartilage endplate (LCE), nucleus pulposus (NP), annulus fibrosus (AF), and AF-support. The IVD scaffold was fabricated using a 3D bioprinting machine (Regenove Bio-Printer-WS, Hangzhou). The printing process was as follows: the 3D model was imported to the system, and printing paths were set for each of the five parts of the model. The different parts of the model was printed using different materials and different paths (the parts of model corresponding to UCE, LCE, and AF-support were printed using PCL polymer [molecular weight = 45000, Sigma], while the parts of model corresponding to AF and NP were printed using the 3D bioprinting inks [CTGF/BMSCs ink and TGF-β3/BMSCs ink, respectively]). PCL was loaded into a metal syringe and heated to 85 ˚C for melting. The CTGF/BMSCs ink and TGF-β3/BMSCs ink were loaded into two plastic syringes, respectively. During the printing process, the 3D bioprinting ink was injected through a 330-μm Teflon nozzle at 50 KPa of air pressure (the air was sterilized, and the printing temperature was 20 ˚C). The PCL was injected through a 330 μm metal nozzle at 450 KPa of air pressure (the air was sterilized, and the printing temperature was 80 ˚C). The layer highlight was 300 μm, and the printing speed was 10 mm/s. All of the experimental procedures were performed under sterile conditions, and the 3D bioprinting machine was sterilized under UV light for 30 min before printing. The diameter of the IVD scaffold was 14 mm and the height was 4 mm. The printed 3D IVD scaffold was crosslinked in a calcium chloride solution (w/v, 5%) at room temperature for 10 min. Then, the scaffold was washed with PBS solution three times, and the PBS solution was subsequently replaced with culture medium.

2.6. Morphology and mechanical property characterization of the bioprinted IVD scaffold

The cross-section and surface morphology of the printed IVD scaffold (without BMSCs) were characterized using a stereomicroscopic (LEICA) and SEM. Before SEM, the samples were fixed in 4% paraformaldehyde for 2 h, followed by dehydration in a gradient of ethanol solution (50%, 70%, 90%, 95%, and 100%). For mechanical property characterization, the printed IVD scaffold was subjected to vertical and lateral compression in a cyclic compression experiment. The deformation history and strain-stress cyclic curve were obtained, and the maximum stress and Young's modulus were calculated.

2.7. Dual GF distribution and release behavior characterization

To characterize the distribution of CTGF and TGF-β3 on the bioprinted IVD scaffold, the GFs were labeled with fluorescein isothiocyanate (FITC) and Rhodamine dyes, respectively (FITC-labeled CTGF and Rhodamine-labeled TGF-β3). In brief, CTGF/TGF-β3 phase solution was reacted with FITC/Rhodamine solution dissolved in DMSO for 12h, and then dialyzes to remove the un-conjugated fluorescent dyes to obtain the FITC-labeled CTGF and Rhodamine-labeled TGF-β3. The 3D-bioprinted IVD scaffold was observed under an inverted fluorescence microscope. The characterization of the release behavior of CTGF (or TGF-β3) from CTGF@PDA NPs (or TGF-β3@PDA NPs) was performed as follows: briefly, 10 mg of CTGF@PDA NPs (or TGF-β3@PDA NPs) was soaked in 10 mL of PBS solution and then incubated at 37 ˚C. At each time point (days 1, 3, 5, 7, 14, 21, 28, and 35), 2 mL of supernatant was removed from the vial and replaced with an equal volume of fresh PBS solution. The amount of sustained-released GFs in the collected medium was measured using the corresponding ELISA Kit, and the drug release curve was eventually plotted. Each sample was assayed in triplicate.

2.8. Cell viability

The printed IVD scaffold was cultured at 37 ˚C and 5% CO_2, with medium changed daily. Cell viability was quantitatively and qualitatively characterized using the Cell Counting Kit (CCK; Sigma-Aldrich Co., Ltd, USA) and Live/Dead Cell Double Staining Kit (Sigma-Aldrich Co., Ltd, USA), respectively. In brief, after 1, 3, 5, and 7 days of culture, the old medium was removed, the fresh medium (DMEM/F-12 medium without FBS and penicillin-streptomycin formulation) and CCK reagent was added and incubated for 30 min at 37 ˚C, followed by measurement of absorbance at 450 nm. After seven days in culture, BMSCs were stained with Calcein-AM/Propidium Iodide (Cal-AM/PI) dye and observed under a fluorescence microscope.

2.9. Cell differentiation

To assess the differentiation of BMSCs loaded onto the 3D-bioprinted IVD scaffold, the gene expression levels of Col I, Col II, and aggrecan were separately examined using real-time quantitative polymerase chain reaction (RT-qPCR). In brief, the 3D-bioprinted IVD scaffold was cultured in media containing the chondrogenic induction supplements (ascorbic acids [50 μg/ml], 1% 1× ITS + 1 solution, sodium pyruvate [100 μg/ml], L-ascorbic acid 2-phosphate [50 μg/ml], L-proline [40 μg/ml], and 0.1 μM dexamethasone). After four weeks of treatment, the cell samples were harvested from the AF region (AF

group) and the NP region (NP group), respectively. A negative control group of BMSCs cultured without any supplements (control group) and two positive control groups of BMSCs cultured with chondrogenic induction supplements and CTGF or TGF-β3 (CTGF group and TGF-β3 group, respectively) were included. Total RNA of each group was isolated and converted to cDNA using reverse transcriptase (Applied Systems, Foster City, CA, USA). RT-PCR was performed in the Applied Biosystems 7300 using Taqman primers and probes specific for glyceraldehyde-3-phosphate dehydrogenase (GAPDH) and other relevant genes. The relative gene expression was calculated using the $2^{-\Delta\Delta Ct}$ method with GAPDH as the reference gene.

2.10. Subcutaneous surgery in nude mice

Three types of IVD scaffolds were printed by 3D bioprinting technology as described above for the animal experiments, including a pure IVD scaffold (without cells and without GFs), a cells/IVD scaffold (empty PDA NPs without GFs but with BMSCs), and a dual-GFs/cells/IVD scaffold (with CTGF and TGF-β3, with BMSCs). Following approval of the Institutional Animal Care and Use Committee at Shanghai Jiao Tong University School of Medicine, athymic nude mice were anesthetized, and the scaffolds were implanted into the dorsum subcutaneous of the mice (n = 10). No complications or adverse reactions were observed after surgery. At 12 weeks postimplantation, the animals were sacrificed under anesthesia, and the specimens were harvested and fixed in 4% paraformaldehyde.

2.11. Histological and immunological characterization of AF reconstruction

The harvested and fixed specimens were embedded in paraffin and cross-sectioned in the upper, middle and lower layers. The slices were stained with hematoxylin-eosin (HE), alcian blue (AB), picrosirius red (PR), and Masson, respectively. Then, the results of the staining were observed by fluorescence microscopy (IX71, Olympus, Japan). The percentage of positive area stained with AB and PR was measured using the Image-Pro Plus software. For immunohistochemistry, the sections were incubated with the respective primary antibody (rabbit anti-Col I antibody [1:200; Sigma, USA] and rabbit anti-Col II antibody [1:100; Abcam, UK]) overnight at 4 °C. All the procedures that followed were performed according to the standard protocol. Briefly, the samples were incubated with horseradish peroxidase (HRP)-labeled secondary antibody (DAKO, K5007) for 50 min, then the sections were further processed with the diaminobenzene (DAB) regent kit (DAKO, K5007) for visualization. Finally, the immunostained samples were viewed with inverted fluorescence microscopy (IX71, Olympus, Japan), and the positive areas were quantified for the analysis of tissue reconstruction.

2.12. Statistical analysis

All quantitative data were expressed as a mean ± standard deviation. The statistical analysis was carried out using one-way ANOVA, followed by Bonferroni's test for the evaluation of specific differences using the Origin 9.1 software (Originlab Corp., Northampton, MA, USA). A value of (*) $P < 0.05$ was considered significant and a value of (**) $P < 0.01$ was considered highly significant.

3. Results

3.1. Preparation of PDA NPs and loading of GFs on PDA NPs

PDA NPs were obtained by oxidative polymerization of DA monomers (Fig. 1a). The reaction conditions and parameters of the oxidative polymerization were determined through preliminary experiments: DA monomer concentration was 10 mg/mL, pH value of reaction solution was 9, and the reaction time was 9 h. After the reaction, the morphology and diameter distribution of the PDA NPs were characterized using SEM and laser particle size analyzer (Fig. 1b and c). The results showed that the PDA NPs had smooth and uniform nanogranular morphology, and the diameter was 324.2 ± 13.9 nm. And the loading efficiency of CTGF and TGF-β3 on PDA NPs was 70.04 ± 0.94% and 72.34 ± 1.06%.

3.2. Characterization of PDA NPs GFs-loaded PDA NPs

After the loading of CTGF/TGF-β3, all of the samples (including DA, PDA NPs, CTGF@PDA NPs, and TGF-β3@PDA NPs) were characterized by FTIR and RS. The FTIR results are shown in Fig. 1d. A wide absorption peak at 3500–3000 cm^{-1} was observed for DA, which corresponded to the OH, NH, and NH_2 stretching vibrations of the DA molecule. The sharp peaks at 2811 cm^{-1} and 1610 cm^{-1} corresponded to the CH_2 and C═C stretching vibrations of DA, respectively. Following oxidative polymerization and subsequent grafting of GFs, absorption peaks at 3430, 2929, and 1629 cm-1 were observed for PDA NPs, CTGF@PDA NPs, and TGF-β3@PDA NPs, which corresponded to the same groups as in the DA molecule. The occurrence of peak shifts and association might be due to the oxidative polymerization reaction. The FTIR curves of DA showed many sharp peaks at 1500–1000 cm^{-1}, which corresponded to the skeleton vibrations of aromatic rings in DA, and these absorption peaks were associated with each other due to the polymerization reaction. Finally, only an absorption peak at 1083 cm^{-1} was observed in DA, confirming the successful synthesis of the PDA NPs. In addition, the FTIR curves of CTGF@PDA NPs and TGF-β3@PDA NPs showed a more significant absorption peak at 1263 cm^{-1} compared with PDA NPs without GFs. This peak was attributed to the stretching vibration of the amide bond, the presence of which proved that CTGF/TGF-β3 was successfully grafted onto the PDA NPs via the formation of amide bonds through EDC/NHS grafting. The RS results were similar and in line with the above conclusions (Fig. 1e). Firstly, the absorption peak of DA at 1617 cm^{-1} was resulted from the C═C bond stretching vibration, and many sharp peaks at 1500–1000 cm^{-1} corresponded to aromatic ring skeleton vibration. Secondly, after oxidative polymerization, only two prominent peaks were observed in PDA NPs, at 1572 and 1415 cm^{-1}, which corresponded to the C═C bond and aromatic ring skeleton vibration, respectively. In addition, in CTGF@PDA NPs and TGF-β3@PDA NPs, three small peaks were observed at 500–550 cm^{-1}, which corresponded to disulfide bonds (S–S) in proteins or polypeptides [26,27]. According to literature reports, various disulfide bonds exist in CTGF/TGF-β3 for maintaining the biological activity of these GFs.

3.3. Preparation of IVD scaffold by 3D bioprinting

The prepared CTGF@PDA NPs and TGF-β3@PDA NPs were mixed with hydrogel and cells to obtain the 3D-bioprinting ink. The cells used in this study were BMSCs obtained from SD rats. The prepared CTGF@PDA NPs and TGF-β3@PDA NPs were mixed with hydrogel and BMSCs to obtain the 3D bioprinting ink for CTGF/BMSCs and TGF-β3/BMSCs, respectively. Before 3D bioprinting, the 3D model of the IVD scaffold was designed using a 3D modeling software. The models consisted of five parts, which corresponded to the UCE, LCE, NP, AF, and AF-support (Fig. 2a). The parts of the model corresponding to the UCE, LCE, and AF-support were printed using PCL polymer. The printing path of IVD scaffold is shown in Fig. 2b. A 3D bioprinter (Fig. 2c) was used to print the IVD scaffold layer by layer, and the printing process is shown in Fig. 2d. Firstly, molten PCL was used to print the LCE layer (the diameter and height were 14 mm and 0.5 mm, respectively). Secondly, the PCL, CTGF/BMSCs ink, and TGF-β3/BMSCs ink were used to print the AF-support, AF, and NP, respectively (the diameter and height were 14 mm and 3 mm, respectively). Finally, the UCE layer was printed similarly as the LCE layer with PCL (the diameter and height were 14 mm and 0.5 mm, respectively). In the end, the 3D-bioprinted dual GF–releasing IVD scaffold was successfully printed for subsequent

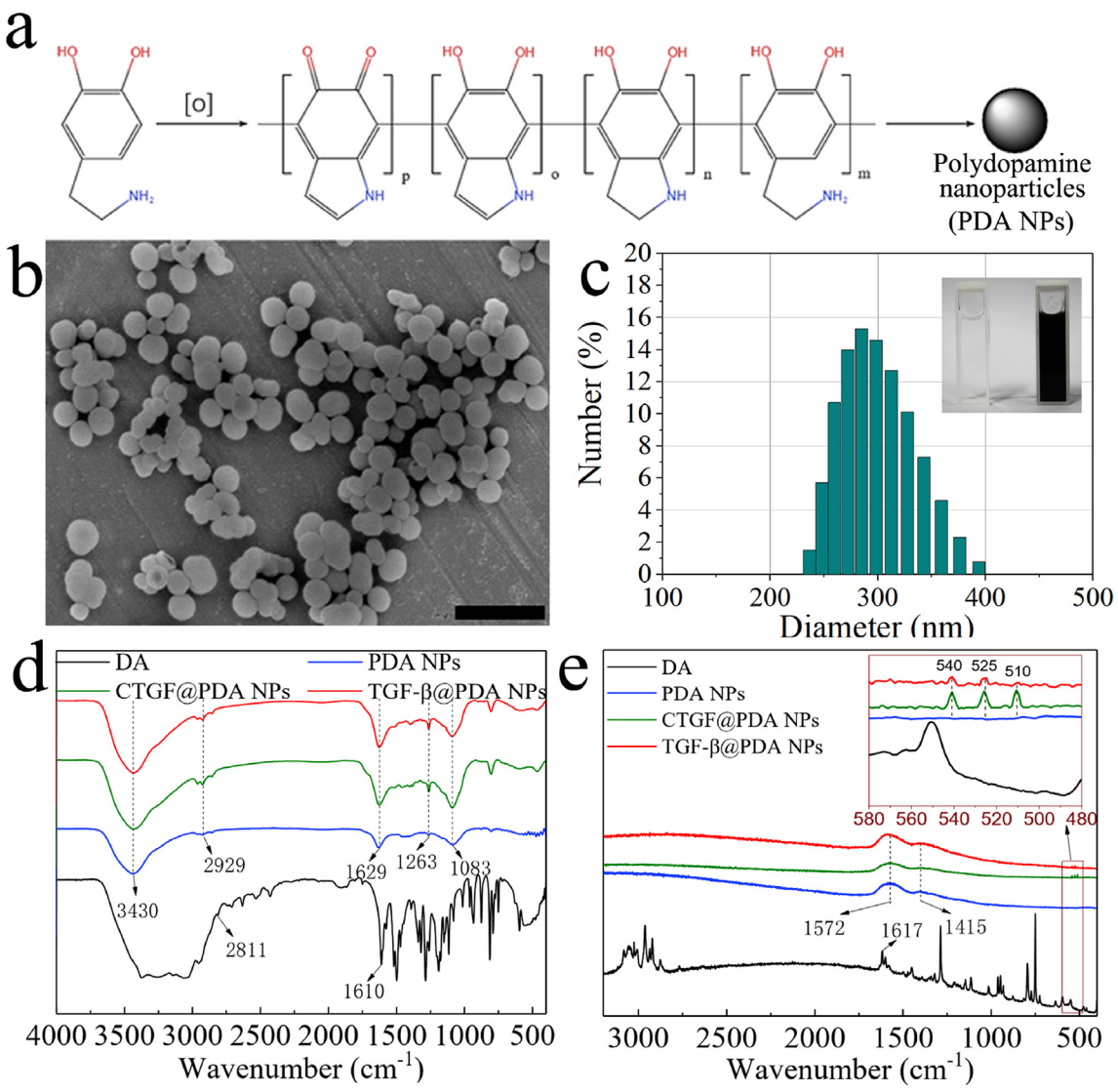

Fig. 1. Polydopamine nanoparticles (PDA NPs) synthesis and characterization. a) Chemical formula for oxidative polymerization of PDA NPs. b) Scanning electron microscope (SEM) images of the PDA NPs. c) The diameter distribution of the PDA NPs (the upper right corner shows the solution state before and after oxidative polymerization of PDA NPs). d) Fourier transform infrared spectroscopy (FTIR) results for dopamine (DA), PDA NPs, CTGF@PDA NPs, and TGF-β3@PDA NPs. e) Raman spectroscopy (RS) results of DA, PDA NPs, CTGF@PDA NPs, and TGF-β3@PDA NPs. Scale bar: (b) = 1 μm.

experiments.

3.4. Morphology and mechanical properties of dual GFs-releasing IVD scaffold

The morphology and mechanical properties of the dual GF–releasing IVD scaffold were characterized. The gross morphology and micromorphology of the IVD scaffold are shown in Fig. 3a–d. The results showed that the printed IVD scaffold had a similar morphology as the designed model (Fig. 3a and b). The bioink-containing PDA NPs and BMSCs successfully filled in the gaps in the PCL framework (Fig. 3c), and the PDA NPs and BMSCs were encapsulated by the porous hydrogel (Fig. 3d). Fig. 3e and g showed the stress-strain curves of the printed IVD scaffold when subjected to cyclic vertical and cyclic lateral compressions. The results of the cyclic compression experiment showed that the IVD scaffold exhibited a good compression recovery capability after printing, and this capability was maintained even after 100 compressions (Fig. 3e, g). The Young's modulus of the scaffold was calculated, and the results are shown in Fig. 3f and h. The Young's modulus decreased from 2.0 to 2.5 MPa (at first cycle) to 1.2–1.6 MPa (at 100th cycle) with vertical compressions. However, it was maintained at 1.2–1.6 MPa with lateral compressions.

3.5. Dual GFs releasing behaviors from IVD scaffold

The distribution and release behavior of CTGF/TGF-β3 of the 3D-bioprinted IVD scaffold are shown in Fig. 3i and j. Fluorescent images of the IVD scaffold showed that CTGF and TGF-β3 were distributed evenly in the AF and NP, respectively. Both CTGF and TGF-β3 were continuously released from the IVD scaffold throughout the experimental period. On day one, 4.19 ± 0.11% of CTGF and 2.14 ± 0.10% of TGF-β3 were released, and on day 35, a similar percentage of the two GFs were released (58.51 ± 0.38% of CTGF and 58.57 ± 0.11% of TGF-β3).

3.6. Cells viability and differentiation behavior on IVD scaffold

The viability and proliferation behavior of cells on the 3D-bioprinted IVD scaffold were characterized *in vitro* using the CCK-8 assay and Live/Dead staining, respectively. The results of CCK-8 assay

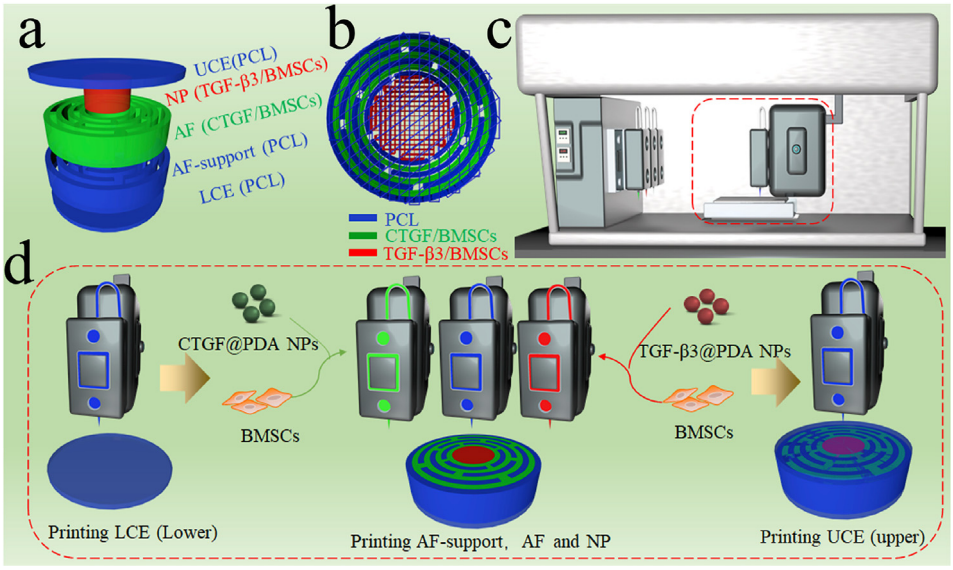

Fig. 2. Fabrication of dual growth factor (GF)–releasing intervertebral disc (IVD) scaffold by 3D bioprinting. a) 3D model of the IVD scaffold. b) 3D printing path of the IVD scaffold. c) 3D bioprinter. d) The print process of 3D-bioprinted IVD scaffold.

showed that 97% of cells were viable on the printed scaffold on day 0. After seven days in culture, the cell viability increased to 99% (Fig. 4a). Live/Dead staining of the 3D-bioprinted IVD scaffold on day 7 also concluded similar results, which showed that most of the cells were living (green) and almost no dead cells (red) were observed (Fig. 4b and c).

After 28 days in culture, *in vitro*-induced differentiation was performed, and the chondrogenic behavior of the scaffold (ability to form fibrocartilage and hyaline cartilage like cells) was examined using qRT-PCR [28,29]. The AF and NP were separated and tested using qRT-PCR, respectively. Fig. 4d–f showed that there were significant differences in the chondrogenic behavior between the control group (BMSCs cultured without any supplements) and other groups (CTGF group: BMSCs differentiated into chondrocytes with the addition of CTGF; TGF-β3 group: BMSCs differentiated into chondrocytes with the addition of TGF-β3; AF group: AF region of the 3D-bioprinted IVD scaffold after induced differentiation; NP group: NP region of the 3D-bioprinted IVD scaffold after induced differentiation). No notable difference in Col I expression was observed between the control group and the NP group, but the AF and CTGF groups expressed significant higher levels of Col I than the other groups (Fig. 4d). On the contrary, higher levels of Col II and aggrecan expression were observed in the NP and TGF-β3 groups than in the control group (Fig. 4e and f).

3.7. Histological evaluation of IVD reconstruction in vivo

Next, we sought to demonstrate the ability of the dual GF–releasing IVD scaffold to promote IVD reconstruction *in vivo*. Three types of fabricated IVD scaffolds (the pure IVD, cells/IVD, and dual-GFs/cells/IVD scaffolds) were implanted, respectively, into the dorsum subcutaneous of nude mice (Fig. 5a). After 3 months, the three types of reconstructed IVD scaffolds were removed for further testing (Fig. 5b). The specimens were sectioned in the upper, middle, and lower layers, and were then stained with HE, Masson, AB, and PR, respectively, for histological evaluation. The results of HE staining revealed that there were lots of reconstructed chondrocytes and cartilage tissue in all three types of implanted IVD scaffolds, and no visible inflammation was observed (Fig. 5c; Figs. S1, S2, ESI). In particular, the HE staining of the middle layer of the cells/IVD and dual-GFs/cells/IVD scaffolds showed better cartilage tissue reconstruction and chondrocyte enrichment than the pure IVD scaffold. In addition, the reconstructed cartilage tissue in the AF and NP regions of the dual-GFs/cells/IVD scaffold was significantly different from the other groups. Specifically, the tissue in the AF was fibrocartilaginous like, but that in the NP was hyaline cartilage like tissue. However, there were no such presentations in the pure IVD and cells/IVD scaffolds. Masson staining (Fig. 5c) showed that the IVD scaffolds had extensive extracellular matrix (ECM; mainly collagen) formation and depositions, and the AF region showed dense fiber morphology. In the upper and lower layers, both HE and Masson staining documented good cartilage tissue formation and abundant ECM secretion in all three types of scaffolds (Figs. S1, S2, ESI).

AB and PR dyes can specifically stain the GAG (to blue) and Col I (to red), respectively (Fig. 6a; Figs. S3a, S4a, ESI). The percentages of AB-positive and PR-positive staining were calculated (Fig. 6b and c; Fig. S3b, c and Fig. S4b, c, ESI). Fig. 6b and c showed that more GAG formation occurred in both the NP and AF regions of the dual-GFs/cells/IVD scaffold than in the same regions of the pure IVD and cells/IVD scaffolds. However, in the NP region, the percentage of PR-positive staining was significantly less in the dual-GFs/cells/IVD scaffold than in the pure IVD and cells/IVD scaffolds. In contrast, in the AF region, the percentage of PR-positive staining was significantly higher in the dual-GFs/cells/IVD and cells/IVD scaffolds than in the pure IVD scaffold. These results indicated that there was less Col I but more Col II formation of dual-GFs/cells/IVD in NP. On the contrary, the Col I formation on the dual-GFs/cells/IVD in the AF was more prominent than that in the pure IVD scaffold and similar to the cells/IVD scaffold.

Next, to confirm the differences in Col formation in each group, immunohistochemical staining of Col I and Col II was performed (Fig. 7; Figs. S5 and S6, ESI). The results showed that in the NP, there were more Col II but less Col I formation in the dual-GFs/cells/IVD scaffold in comparison to the other scaffolds. In the AF, there were more Col I formation in the dual-GFs/cells/IVD scaffold than in the other scaffolds, and more Col II formation in the dual-GFs/cells/IVD and cells/IVD scaffolds than in the pure IVD scaffold.

3.8. Biomechanics characterization of reconstructed IVD

To evaluate the reconstruction of the IVD scaffold *in vivo*, the mechanical function of compression resistance of the three reconstructed IVD scaffolds was characterized in a cyclic compression experiment (Fig. 8), and the Young's modulus of the three scaffolds was calculated (Fig. 8b, d). The vertical compressive Young's modulus of the cells/IVD scaffold (3.05–3.10 MPa) was similar to that of the pure IVD scaffold (3.05–3.20 MPa), while that of the dual-GFs/cells/IVD scaffold

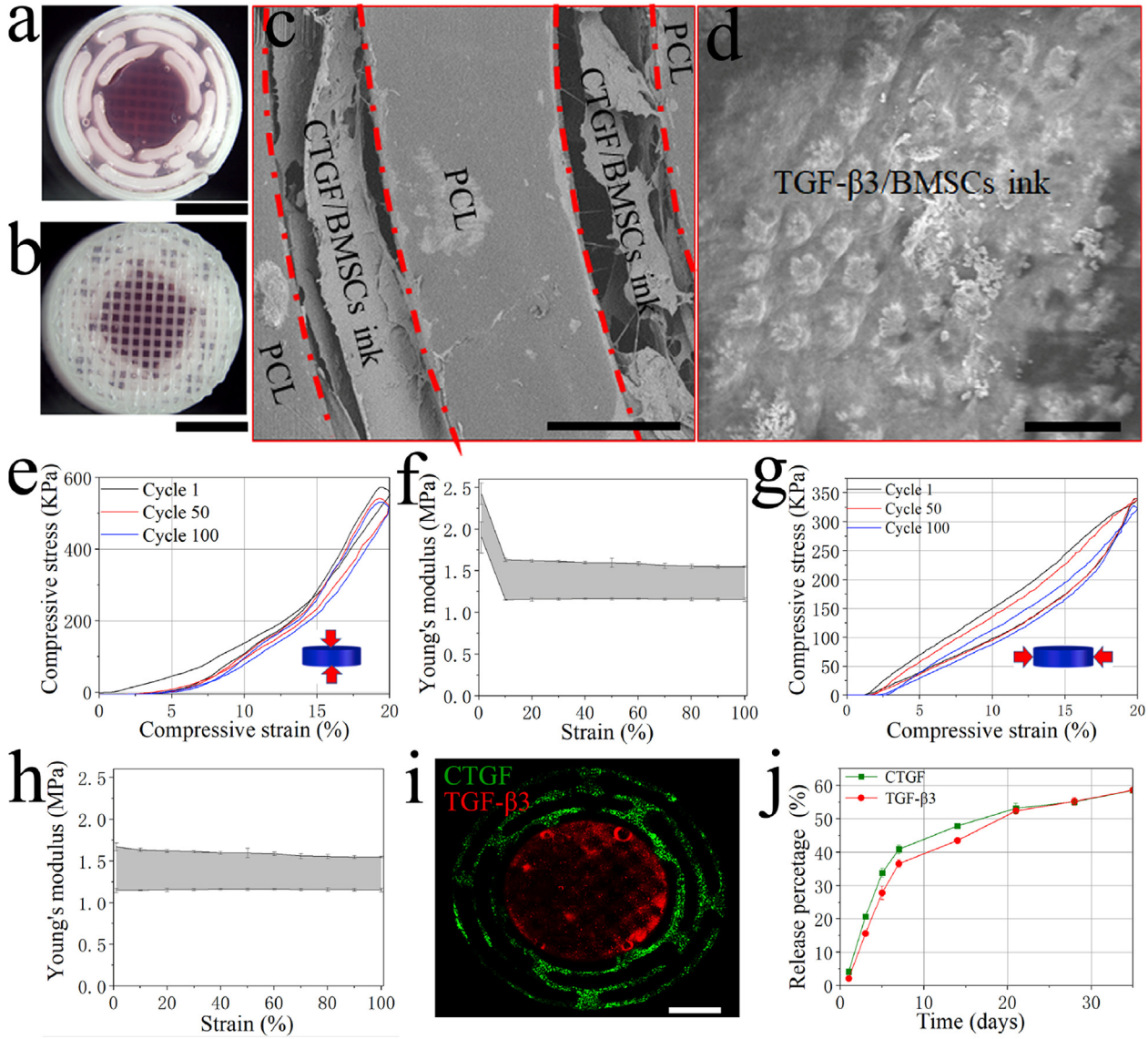

Fig. 3. Characterization of the 3D-bioprinted IVD scaffold. a) Stereomicroscopic image of the mid-section. b) Stereomicroscopic image of the surface. c) SEM image of the AF region. d) SEM image of the NP region. e) Vertical compressive stress-strain curve with different cycles. f) The vertical compressive Young's modulus in 100 cycles. g) Lateral compressive stress-strain curve with different cycles. h) The lateral compressive Young's modulus in 100 cycles. i) Fluorescence images of CTGF (green) and TGF-β3 (red) in the 3D-bioprintied IVD scaffold. j) Release behavior of the two types of GFs from the IVD scaffold. Scale bars: (a) = 5 mm, (b) = 5 mm, (c) = 300 μm, (d) = 20 μm, (i) = 3 mm.

(5.30–5.35 MPa) was higher than the other scaffolds. Similarly, the lateral compressive Young's modulus of the dual-GFs/cells/IVD scaffold (3.10–3.30 MPa) was higher than that of the pure IVD (1.80–2.80 MPa) and cells/IVD (1.80–2.00 MPa) scaffolds.

4. Discussion

In this study, the PDA NPs were successfully synthesized. The characterization of SEM, FTIR and RS indicated that PDA NPs was prepared and have been proven to form uniform nanoparticles via the simple oxidative polymerization of DA monomers [30]. And then CTGF/TGF-β3 was successfully grafted on the PDA NPs. The nanoscale PDA NPs were used as a GF carrier in the present study for two reasons. At first, their nanometer size ensures that the nozzles will not be blocked during the process of 3D bioprinting. Second, PDA NPs are known for their excellent biocompatibility and adhesion properties [31]. The adhesion properties of PDA NPs not only enable GFs but also cells to adhere properly. In other words, the GF–loaded PDA NPs are conducive to adhesion by cells and tissues, thus allowing the delivery of GFs into the organisms and reducing the chance of sudden release.

During the 3D printing process, as a major component of the 3D-bioprinting ink, the hydrogel was prepared by dissolving Gel, HA, and SA in fresh medium to enhance good rheological properties, printability, and biocompatibility. PCL was selected as a mechanical support for the IVD scaffold after melt printing, which is widely used in the field of 3D printing because of its good printability, biodegradability, and biocompatibility [32–34]. In the present study, The parts of the model corresponding to the AF and NP were printed using the 3D bioprinting ink (CTGF/BMSCs ink and TGF-β3/BMSCs ink, respectively), which were used to provide the biofunction of chondrogenesis (formation of fibrochondroctyes like and hyaline chondrocytes like) in the IVD scaffold. and the mechanical support for the IVD scaffold was mainly provided by PCL [35]. After 3D printing, The compression experiment showed no significant change in the printed IVD scaffold, indicating its high compressive strength. The drug releasing results indicated that CTGF and TGF-β3 could be released in a slow and sustained manner,

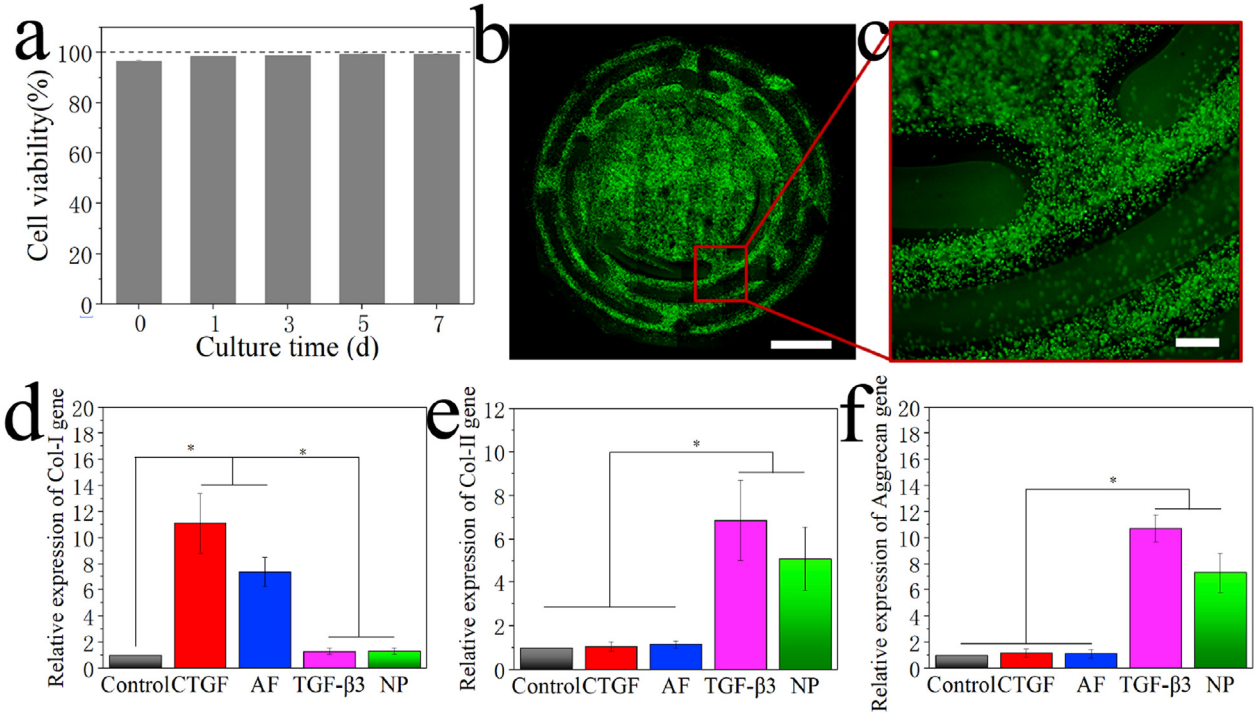

Fig. 4. *In vitro* characterization of the 3D-bioprinted IVD scaffold. a) Cell viability assay of the 3D-bioprinted scaffold after culturing. b) Low-magnification fluorescent image obtained from Live/Dead staining of the 3D-bioprinted scaffold after seven days in culture. c) High-magnification fluorescent image. d) Expression of the Col I gene after induced differentiation in different groups. e) Expression of the Col II gene. f) Expression of the aggrecan gene. Scale bars: (b) = 3 mm, (c) = 100 μm.

and the releasing behaviors for the two types of GFs presented a similar release kinetics. It also suggested that the use of PDA NPs facilitated a highly efficient and simple approach for GF loading [36].

The cell viability results confirmed that BMSCs showed good viability on the IVD scaffold, while the Live/Dead staining results documented that BMSCs could survive well in the bioink. This could be due to two reasons [37]: first, the good biocompatibility of hydrogel promoted cell growth and adhesion; and second, the porous structure of hydrogel was conducive to the metabolism and exchange of nutrients [38,39]. Overall, our findings showed that premixing BMSCs with hydrogel prior to printing of the IVD scaffold not only provided a good means for loading GFs, but also for loading cells. Meanwhile, the *in vitro*

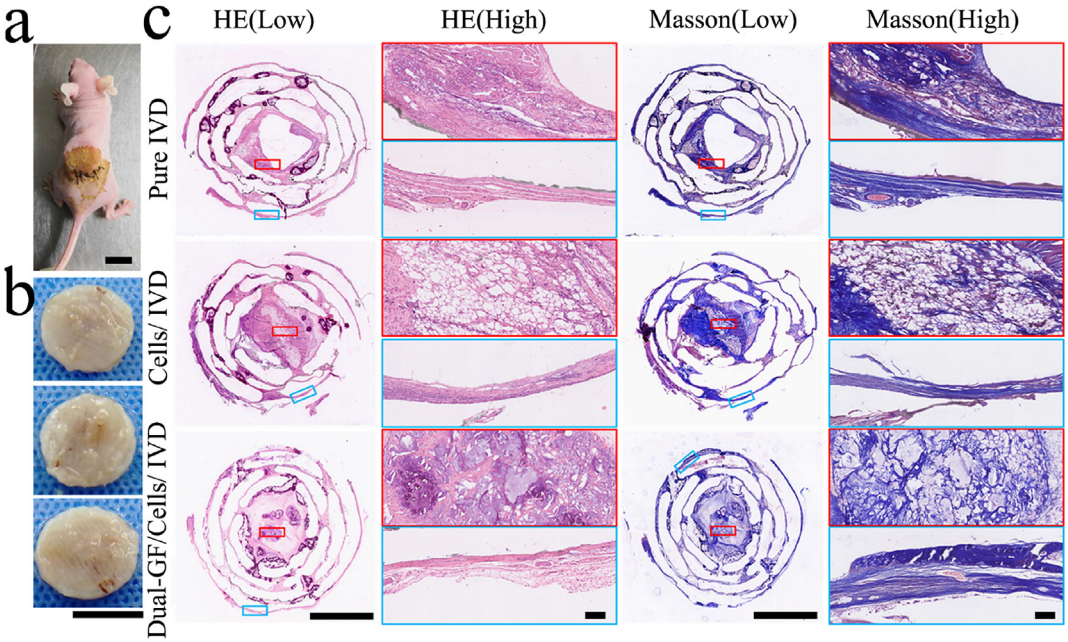

Fig. 5. *In vivo* testing and histological staining of the middle layers of the three types of IVD scaffolds. a) Gross morphology of the IVD scaffolds after subcutaneous implantation in nude mice. b) Digital photos of the three IVD scaffolds six months after implantation (from top to bottom are the pure IVD, cells/IVD and dual-GFs/cells/IVD scaffolds). c) Hematoxylin–eosin (HE) staining and Masson staining of middle layers of the three IVD scaffolds at low and high magnifications. Scale bars: (a) = 10 mm, (b) = 10 mm, (c, low) = 5 mm, (c, high) = 100 μm.

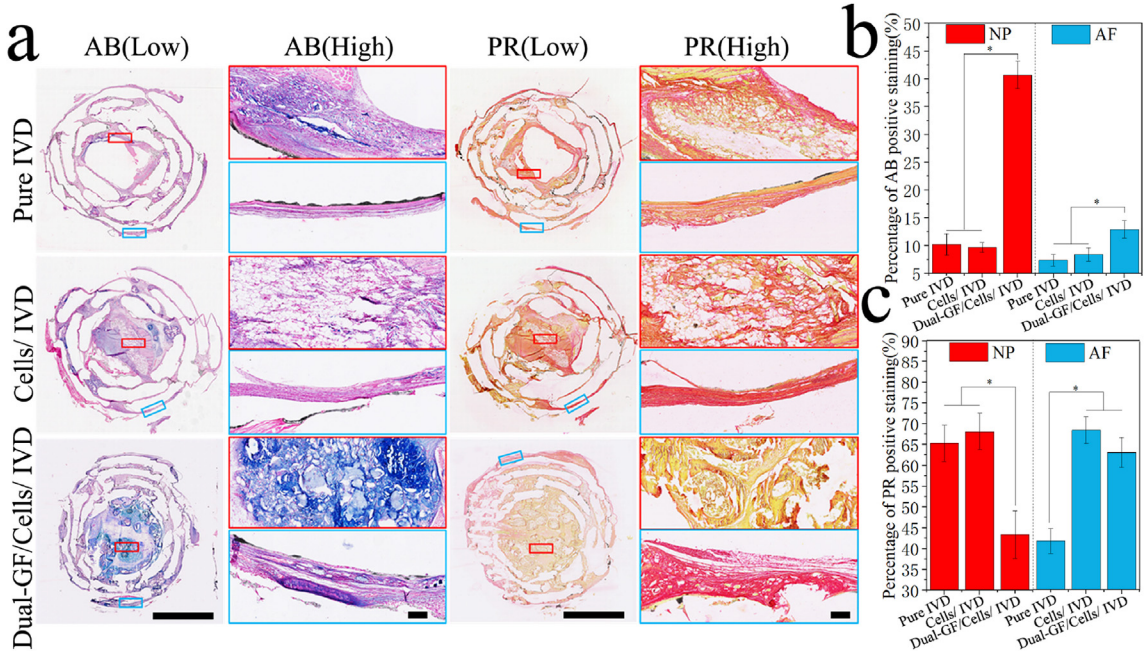

Fig. 6. Histological staining of the middle layers of the three IVD scaffolds with special stains. a) AB staining and PR staining of the middle layers of the three IVD scaffolds at low and high magnifications. b) Statistical results of AB-positive staining of the nucleus pulposus (NP) and annulus fibrous (AF) in the middle layers of the three IVD scaffolds. c) Statistical results of PR-positive staining in the NP and AF in the middle layers of the three IVD scaffolds. Scale bars: (a, low) = 5 mm, (a, high) = 100 μm.

cell differentiation results demonstrated that CTGF was continuously released from the AF, and its bioactivity promoted the differentiation of the BMSCs into fibrocartilage like cells, and the released TGF-β3 from the NP region could promote the differentiation of the BMSCs into hyaline cartilage like cells.

After *in vivo* implantation, the HE and Masson results indicated that BMSCs promoted the IVD reconstruction in the cells/IVD and dual-GFs/cells/IVD scaffolds. The exhibition of zone specific matrix in dual-GFs/cells/IVD scaffold might be attributable to the loading of CTGF in the AF and the TGF-β3 in the NP [40,41]. Usually, normal IVD tissue is composed of two major anatomical regions: the AF and the NP, which are structurally and compositionally different [42]. The main component of the AF region is fibrocartilage, of which the ECM is composed of a large amount of Col I and a small amount of Col II and GAG. Unlike the AF region, the NP region is primarily composed of hyaline cartilage. The NP ECM comprises more Col II and GAG but less Col I than that the AF ECM [43]. The histological staining with AB stains the acidic mucopolysaccharides in the cytoplasm to blue, and is used to stain the GAG

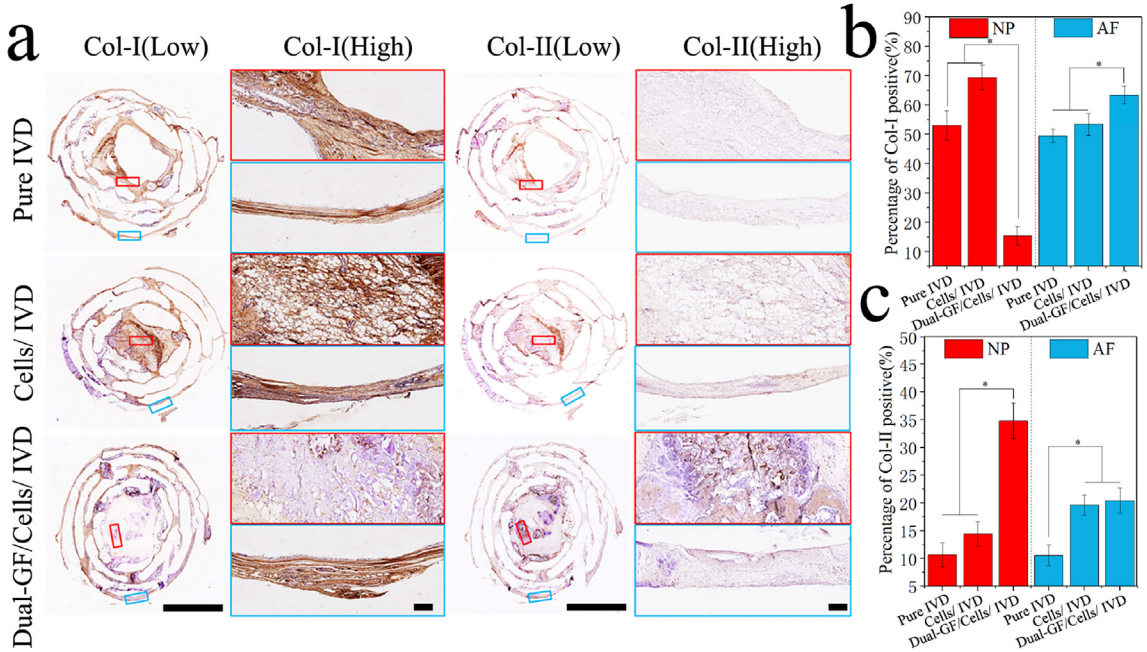

Fig. 7. Immunohistochemistry of the middle layers of the three IVD scaffolds. a) Results of immunohistochemical staining of the middle layers of the three IVD scaffolds at low and high magnifications. b) Statistical results of Col I-positive staining of the NP and AF in the middle layers of the three IVD scaffolds. c) Statistical results of Col II-positive staining of the NP and AF in the middle layers of the three IVD scaffolds. Scale bars: (a, low) = 5 mm, (a, high) = 100 μm.

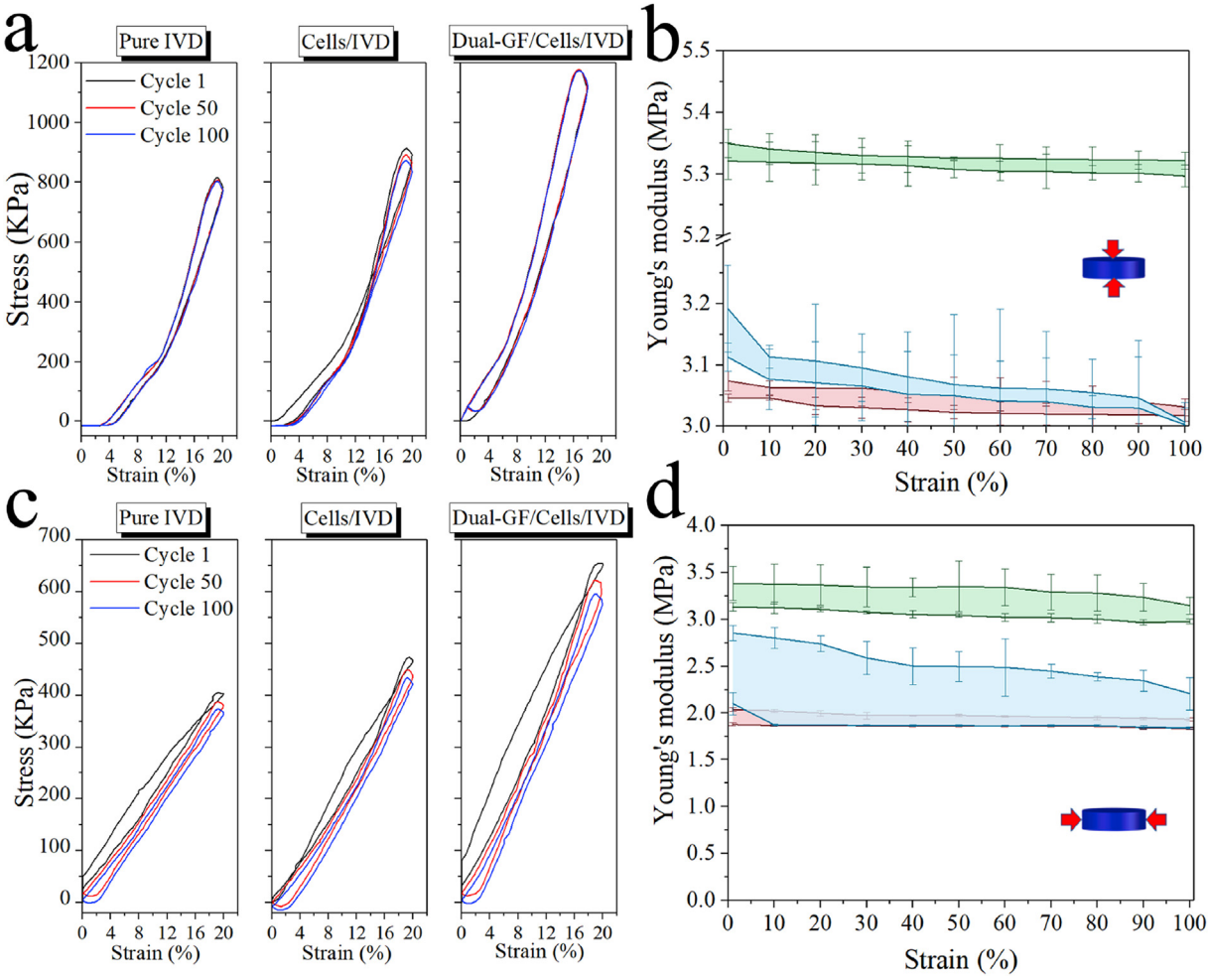

Fig. 8. Compression mechanics characterization of the three reconstructed IVD scaffolds three months after transplantation. a) Vertical compressive stress-stain curves with different cycles. b) The vertical compressive Young's modulus in 100 cycles. c) Lateral compressive stress-stain curves with different cycles. d) The lateral compressive Young's modulus in 100 cycles.

in cartilage tissue [44]. PR is a strong acid anionic dye that specifically stains collagen in the ECM, and different collagen fibers are stained to different colors due to the phenomenon of double refraction [45]. Since the GAG will become blue after staining with AB, and the Col I and Col II will become red and yellow, respectively, after staining with PR, the reconstruction and formation of hyaline cartilage like tissue and fibrocartilage like tissue can be well-distinguished by these two special histological stains. In addition, the immunohistochemistry of Col I and Col II was used to evaluate the zone specific matrix of constructed IVD. Collectively, these results indicated that the addition of BMSCs via 3D bioprinting could promote Col I formation in the IVD scaffolds; the addition of TGF-β3 could promote the formation of GAG and Col II in the NP; and the addition of CTGF could promote the formation of GAG and Col I in the AF. The corresponding statistical analyses of the AB and PR staining on the three types of scaffolds in the upper and lower layers showed similar results (Figs. S3 and S4, ESI). Both the upper and lower layers of the cells/IVD scaffold exhibited more Col I formation than the pure IVD scaffold, and the dual-GFs/cells/IVD scaffold exhibited more GAG and less Col I formation than the pure IVD and cells/IVD scaffolds. Interestingly, although the upper and lower layers of the IVD scaffolds were not printed with BMSCs and GFs during the 3D bioprinting process, differences still existed in the reconstructed tissues between the dual-GFs/cells/IVD and pure IVD scaffolds. This might be due to the cell migration and GF-release from the middle layer of the dual-GFs/cells/IVD scaffold to the upper and lower layers. These observations suggested that the released TGF-β3 could promote Col II formation in the NP, while the released CTGF could promote Col I formation in the AF. These results not only confirmed the histological staining results obtained earlier in this study, but were also consistent with the observations in previous reports [20]. In fact, protrusion of IVD is resulted from AF rupture under the action of external forces, which causes protrusion (or prolapse) of the NP. Therefore, optimal IVD reconstruction should include both AF reconstruction and NP reconstruction. However, AF and NP have different structures, components, and functions. In the present study, our findings confirmed that the dual-GFs/cells/IVD scaffold could promote IVD reconstruction into two types of tissues with different components and structures.

In the end, the mechanical results indicated that by loading BMSCs and dual GFs, the Young's modulus of the dual-GFs/cells/IVD scaffold increased and was close to that of native IVD tissue, while the compression modulus of native IVD tissue was 6.7 ± 2.7 MPa [46]. This could facilitate the performance of biological functions, such as absorbing mechanic shock and withstanding pressure, by the reconstructed IVD.

As a kind of tissue with complex structure and function, the application of intervertebral disc scaffolds is not only *in vitro* cell level and subcutaneous characterization of nude mice. The evaluation in large mammal animal models is necessary. This is a limitation of this study. However, due to the complexity and time-consuming of spinal surgery in large animals (such as sheep and dogs), we are trying to further animal research, hoping to better evaluate the application potential of the IVD scaffold. In addition, the gene expression markers of NP and AF

cells and the Poisson's ratio of reconstructed IVD are also important to evaluate our research conclusion. This is another limitation of our study.

5. Conclusion

In the present study, the dual GF–releasing IVD scaffold was fabricated by 3D bioprinting technology. First, PDA NPs were fabricated as uniform nanospheres with diameter of 324.2 ± 13.9 nm, and FTIR and RS characterization confirmed that dual GFs (CTGF and TGF-β3) were successfully loaded onto the surface of the PDA NPs. Then, both CTGF@PDA NPs and TGF-β3@PDA NPs were mixed with BMSCs to print the AF and NP regions of the IVD scaffold, while the biomaterial PCL was used to print the framework of the IVD scaffold. The fluorescence images and results on release behaviors confirmed that both CTGF and TGF-β3 were uniformly distributed and continuously released from the different parts of the IVD scaffold. Mechanical experiments demonstrated that the printed IVD scaffold could maintain strong compression strength after 100 compressions. *In vitro* testing confirmed that the printed BSMCs maintained high levels of viability and were able to differentiate into pulposus like cells and annulus fibrosus like cells upon induction with the two types of released GFs, respectively. Finally, *in vivo* experiments confirmed that the reconstructed IVD scaffold exhibited a zone-specific matrix phenotype, as demonstrated by histological and immunological characterization. In summary, the 3D-bioprinted, dual GF–releasing IVD scaffold showed great potential for clinical application. However, the evaluation in large mammal animal models needs to be further studied.

Author contributions

Binbin Sun, Zhiguang Qiao and Kerong Dai designed the research. Binbin Sun carried out the materials and characterization. Binbin Sun, Meifei Lian and Yu Han conducted the cell experiments. Binbin Sun and Zhiguang Qiao conducted the animal surgeries. Binbin Sun and Kerong Dai drafted the manuscript. Wenbo Jiang and Xiumei Mo designed and supported the research. All authors read and approved the final manuscript.

work reported in this paper.

Declaration of competing interestCOI

The authors declare no conflict of interest.

CRediT authorship contribution statement

Binbin Sun: Methodology, Investigation, Writing - original draft. **Meifei Lian:** Investigation. **Yu Han:** Investigation. **Xiumei Mo:** Conceptualization, Resources, Writing - review & editing. **Wenbo Jiang:** Conceptualization, Resources. **Zhiguang Qiao:** Conceptualization, Resources, Writing - review & editing. **Kerong Dai:** Supervision, Writing - review & editing.

Acknowledgements

This research was supported by National Key R&D Program of China (No. 2018YFB1105600,No.2018YFA0703000), National Natural Science Foundation of China (No. 81802131), Project funded by China Postdoctoral Science Foundation (No. 2019T120347) and the fund of No. XK2019013.

Appendix A. Supplementary data

Supplementary data related to this article can be found at https://doi.org/10.1016/j.bioactmat.2020.06.022.

Reerences

[1] March Lyn, U.R. Smith Emma, G. Hoy Damian, J. Cross Marita, Sanchez-riera Lidia,Blyth Fiona,Buchbinder Rachelle,Vos Theo,Woolf Anthony D., burden of disability due to musculoskeletal (MSK) disorders, Best Pract. Res. Clin. Rheumatol. 28 (3) (2014) 353–366.
[2] Mugdha Gore, Sadosky Alesia, R. Stacey Brett, Tai Kei-Sing,Leslie Douglas, the burden of chronic low back pain: clinical comorbidities, treatment patterns, and health care costs in usual care settings, Spine 37 (11) (2012) E668–E677.
[3] Wei Jiangbo, Yueming Song, Lin Sun, Chaoliang Lv, Comparison of artificial total disc replacement versus fusion for lumbar degenerative disc disease: a meta-analysis of randomized controlled trials, Int. Orthop. 37 (7) (2013) 1315–1325.
[4] K. Resnick Daniel, William C. Watters, Lumbar disc arthroplasty: a critical review, Clin. Neurosurg. 54 (2007) 83.
[5] S. Harrop James, A. Youssef Jim, Maltenfort Mitch, Vorwald Peggy, Jabbour Pascal, M. Bono Christopher, Goldfarb Neil, R. Vaccaro Alexander, S. Hilibrand Alan, Lumbar adjacent segment degeneration and disease after arthrodesis and total disc arthroplasty, Spine 33 (15) (2008) 1701–1707.
[6] Clouet Johann, Fusellier Marion, Camus Anne, Visage Catherine Le, Guicheux Jérôme, Intervertebral disc regeneration: from cell therapy to the development of novel bioinspired endogenous repair strategies, Adv. Drug Deliv. Rev. 146 (2019) 306–324.
[7] P.G. Urban Jill, Smith Stanton, C.T. Fairbank Jeremy, Nutrition of the intervertebral disc, Spine 29 (23) (2004) 2700–2709.
[8] R.S. Bibby Susan, A. Jones Deborah, M. Ripley Ruth, P.G. Urban Jill, Metabolism of the intervertebral disc: effects of low levels of oxygen, glucose, and pH on rates of energy metabolism of bovine nucleus pulposus cells, Spine 30 (5) (2005) 487–496.
[9] D. Bowles Robby, H. Gebhard Harry, Härtl Roger, J. Bonassar Lawrence, Tissue-engineered intervertebral discs produce new matrix, maintain disc height, and restore biomechanical function to the rodent spine, Proc. Natl. Acad. Sci. Unit. States Am. 108 (32) (2011) 13106–13111.
[10] Yong-Can Huang, Yong Hu, Zhen Li, D.K. Luk Keith, Biomaterials for intervertebral disc regeneration: current status and looming challenges, J. Regen. Med. Tissue Eng. 12 (11) (2018) 2188–2202.
[11] Junchuan Yang, Le Wang, Wei Zhang, Zhen Sun, Li Ying, Mingzhu Yang, Di Zeng, Baogan Peng, Wenfu Zheng, Xingyu Jiang, Reverse reconstruction and bioprinting of bacterial cellulose-based functional total intervertebral disc for therapeutic implantation, Small 14 (7) (2018) 1702582.
[12] M. Richardson Stephen, Kalamegam Gauthaman, N. Pushparaj Peter, Matta Csaba, Adnan Memic, Khademhosseini Ali, Mobasheri Reza, L. Poletti Fabian, A. Hoyland Judith, Mobasheri Ali, Mesenchymal stem cells in regenerative medicine: focus on articular cartilage and intervertebral disc regeneration, Methods 99 (2016) 69–80.
[13] Jukka Tolonen, Grönblad Mats, Virri Johanna, Seitsalo Sappo, Rytömaa Tapio, Karaharju Erkki, Basic fibroblast growth factor immunoreactivity in blood vessels and cells of disc herniations, Spine 20 (3) (1995) 271–276.
[14] Takae Reiko, Matsunaga Shunji, Origuchi Nobuo, Takuya Yamamoto, Norio Morimoto, Shusaku Suzuki, Sakou Takashi immunolocalization of bone morphogenetic protein and its receptors in degeneration of intervertebral disc, Spine 24 (14) (1999) 1397.
[15] T. Konttinen Yrjö, Kemppinen Pertti, Li Tian-Fang, Waris Eero, Pihlajamäki Harri, Sorsa Timo, Michiaki Takagi, Santavirta Seppo, G.S. Schultz, M.G. Humphreys-Beher, Transforming and epidermal growth factors in degenerated intervertebral discs, J. Bone Jt. Surg. Br. Vol. 81 (6) (1999) 1058–1063.
[16] J. Du, R.G. Long, T. Nakai, D. Sakai, L.M. Benneker, G. Zhou, B. Li, D. Eglin, J.C. Iatridis, M. Alini, Functional cell phenotype induction with TGF-β1 and collagen-polyurethane scaffold for annulus fibrosus rupture repair, Eur. Cell. Mater. 39 (2020) 1.
[17] Tomoko Nakai, Daisuke Sakai, Yoshihiko Nakamura, Nukaga Tadashi, Grad Sibylle, Zhen Li, Alini Mauro, Danny Chan, Koichi Masuda, Kiyoshi Ando, CD146 defines commitment of cultured annulus fibrosus cells to express a contractile phenotype, J. Orthop. Res. 34 (8) (2016) 1361–1372.
[18] Meisel Hans Jörg, Siodla Vilma, Ganey Timothy, Minkus Yvonne, William C. Hutton, J. Alasevic Olivera, Clinical experience in cell-based therapeutics: disc chondrocyte transplantation: a treatment for degenerated or damaged intervertebral disc, Biomol. Eng. 24 (1) (2007) 5–21.
[19] S. Hwang Nathaniel, Shyni Varghese, Puleo Christopher, Zijun Zhang, Elisseeff Jennifer, Morphogenetic signals from chondrocytes promote chondrogenic and osteogenic differentiation of mesenchymal stem cells, J. Cell. Physiol. 212 (2) (2007) 281–284.
[20] H. Lee Chang, A. Rodeo Scott, Fortier Lisa Ann,Lu Chuanyong,Erisken Cevat,Mao Jeremy J., Protein-releasing polymeric scaffolds induce fibrochondrocytic differentiation of endogenous cells for knee meniscus regeneration in sheep, Sci. Transl. Med. 6 (266) (2014) 266ra171-266ra171.
[21] Yanlan Liu, Kelong Ai, Jianhua Liu, Mo Deng, Yangyang He, Lehui Lu, Dopamine-melanin colloidal nanospheres: an efficient near-infrared photothermal therapeutic agent for in vivo cancer therapy, Adv. Mater. 25 (9) (2013) 1353–1359.
[22] Kang Hyun-Wook, Sang Jin Lee, Ko In Kap, Kengla Carlos, J. Yoo James, Atala Anthony, A 3D bioprinting system to produce human-scale tissue constructs with structural integrity, Nat. Biotechnol. 34 (3) (2016) 312–319.
[23] M. Jessop Zita, Al-Sabah Ayesha, D. Gardiner Matthew, Combellack Emman, Karl Hawkins, S. Whitaker Iain, 3D bioprinting for reconstructive surgery: principles, applications and challenges, J. Plast. Reconstr. Aesthetic Surg. 70 (9) (2017) 1155–1170.
[24] Weijie Peng, Pallab Datta, Ayan Bugra, Ozbolat Veli, Sosnoski Donna, T. Ozbolat Ibrahim, 3D bioprinting for drug discovery and development in pharmaceutics,

Acta Biomater. 57 (2017) 26–46.
[25] Duo Hu, Dongwei Wu, Lin Huang, Yanpeng Jiao, Lihua Li, Lu Lu, Changren Zhou, 3D bioprinting of cell-laden scaffolds for intervertebral disc regeneration, Mater. Lett. 223 (2018) 219–222.
[26] Chih-Hsien Wang, Chia-Chi Huang, Long-Liu Lin, Wenlung Chen, The effect of disulfide bonds on protein folding, unfolding, and misfolding investigated by FT–Raman spectroscopy, J. Raman Spectrosc. 47 (8) (2016) 940–947.
[27] Mong Liang, Y.T. Chen Vivin, Hsiu-Ling Chen, Wenlung Chen, A simple and direct isolation of whey components from raw milk by gel filtration chromatography and structural characterization by Fourier transform Raman spectroscopy, Talanta 69 (5) (2006) 1269–1277.
[28] V. Perez-Castro Ana, G. Vogel Kathryn, In situ expression of collagen and proteoglycan genes during development of fibrocartilage in bovine deep flexor tendon, J. Orthop. Res. 17 (1) (1999) 139–148.
[29] M. Mueller Stefan, Shortkroff Sonya, O. Schneider Thomas, A. Breinan Howard, V. Yannas Ioannis, Spector Myron, Meniscus cells seeded in type I and type II collagen–GAG matrices in vitro, Biomaterials 20 (8) (1999) 701–709.
[30] Liu Qian, Zonghua Pu, M. Asiri Abdullah, O. Al-Youbi Abdulrahman, Sun Xuping, Polydopamine nanospheres: a biopolymer-based fluorescent sensing platform for DNA detection, Sensor. Actuator. B Chem. 191 (2014) 567–571.
[31] Yanlan Liu, Kelong Ai, Lehui Lu, Polydopamine and its derivative materials: synthesis and promising applications in energy, environmental, and biomedical fields, Chem. Rev. 114 (9) (2014) 5057–5115.
[32] B. Kolesky David, L. Truby Ryan, Gladman A. Sydney, A. Busbee Travis, A. Homan Kimberly, A. Lewis Jennifer, 3D bioprinting of vascularized, heterogeneous cell--laden tissue constructs, Adv. Mater. 26 (19) (2014) 3124–3130.
[33] Helena N. Chia, M. Wu Benjamin, Recent advances in 3D printing of biomaterials, J. Biol. Eng. 9 (1) (2015) 1–14.
[34] Fengyuan Liu, Vyas Cian, Poologasundarampillai Gowsihan, Ian Pape, Hinduja Sri, Mirihanage Wajira, Bartolo Paulo, Structural evolution of PCL during melt extrusion 3D printing, Macromol. Mater. Eng. 303 (2) (2018) 1700494.
[35] W. Hutmacher Dietmar, Schantz Thorsten, Zein Iwan, Kee Woei Ng, Swee Hin Teoh, Kim Cheng Tan, Mechanical properties and cell cultural response of polycaprolactone scaffolds designed and fabricated via fused deposition modeling, J. Biomed. Mater. Res. 55 (2) (2001) 203–216. An Official Journal of The Society for Biomaterials, The Japanese Society for Biomaterials, and The Australian Society for Biomaterials and the Korean Society for Biomaterials.
[36] Kisuk Yang, Lee Jung Seung, Kim Jin, Yu Bin Lee, Heungsoo Shin, Soong Ho Um, Kim Jeong Beom, Kook Park, Haeshin Lee, Cho Seung-Woo, Polydopamine-mediated surface modification of scaffold materials for human neural stem cell engineering, Biomaterials 33 (29) (2012) 6952–6964.
[37] Hospodiuk Monika, Madhuri Dey, Sosnoski Donna, T. Ozbolat Ibrahim, The bioink: a comprehensive review on bioprintable materials, Biotechnol. Adv. 35 (2) (2017) 217–239.
[38] Möller Thomas, Amoroso Matteo, Hägg Daniel, Brantsing Camilla, Rotter Nicole, Apelgren Peter, Lindahl Anders, Kölby Lars, Gatenholm Paul, In vivo chondrogenesis in 3D bioprinted human cell-laden hydrogel constructs, Plast. Reconstr. Surg. Glob. Open 5 (2) (2017).
[39] Bin Zhang, Lei Gao, Long Gu, Huayong Yang, Yichen Luo, Ma Liang, High-resolution 3D bioprinting system for fabricating cell-laden hydrogel scaffolds with high cellular activities, Procedia CIRP 65 (2017) 219–224.
[40] Bianco Paolo, Cao Xu, S. Frenette Paul, J. Mao Jeremy, G. Robey Pamela, J. Simmons Paul, Cun-Yu Wang, The meaning, the sense and the significance: translating the science of mesenchymal stem cells into medicine, Nat. Med. 19 (1) (2013) 35–42.
[41] H. Lee Chang, Bhranti Shah, K. Moioli Eduardo, J. Mao Jeremy, CTGF directs fibroblast differentiation from human mesenchymal stem/stromal cells and defines connective tissue healing in a rodent injury model, J. Clin. Invest. 120 (9) (2010) 3340–3349.
[42] Luoma Katariina, Riihimäki Hilkka, Luukkonen Ritva, Raininko Raili, Viikari-Juntura Eira, Lamminen Antti, Low back pain in relation to lumbar disc degeneration, Spine 25 (4) (2000) 487–492.
[43] Alini Mauro, M. Eisenstein Stephen, Keita Ito, Christopher Little, Kettler A. Annette, Koichi Masuda, Melrose James, Ralphs Jim, Stokes Ian, Wilke Hans Joachim, Are animal models useful for studying human disc disorders/degeneration? Eur. Spine J. 17 (1) (2008) 2–19.
[44] S. Mello Maria Luiza, M. Michelacci Yara, Stockert Juan Carlos, Vidal Benedicto de Campos, Optical anisotropy of alcian blue-stained acid glycosaminoglycans, Acta Histochem. 109 (1) (2007) 78–85.
[45] L. Junqueira, U. Cx̧, G. Bignolas, R. Brentani Ricardo, Picrosirius staining plus polarization microscopy, a specific method for collagen detection in tissue sections, Histochem. J. 11 (4) (1979) 447–455.
[46] L. Showalter Brent, M. Elliott Dawn, Weiliam Chen, R. Malhotra Neil, Evaluation of an in situ gelable and injectable hydrogel treatment to preserve human disc mechanical function undergoing physiologic cyclic loading followed by hydrated recovery, J. Biomech. Eng. 137 (8) (2015).